Supplement of Atmos. Chem. Phys., 23, 9597–9612, 2023
https://doi.org/10.5194/acp-23-9597-2023-supplement

Atmospheric Chemistry and Physics

Supplement of

In-depth study of the formation processes of single atmospheric particles in the south-eastern margin of the Tibetan Plateau

Li Li et al.

Correspondence to: Qiyuan Wang (wangqy@ieecas.cn) and Junji Cao (jjcao@mail.iap.ac.cn)

S1. Characteristics of particle composition

Nine particle groups are identified based on their chemical characteristics shown in the publication. General mass spectral characteristics for each particle group are presented in Fig. S3. The intense potassium ($^{39}K^+$) peak in almost all particles is attributed to the highly sensitive to potassium with the desorption laser used in the SPAMS (Gross et al., 2000; Xu et al., 2017; Giorio et al., 2015). Studies have reported that $^{39}K^+$ by itself isn't an adequate marker for biomass burning because it presents in mass spectra of a variety of particle types (Healy et al., 2013). Moreover, the peak at *m/z* 39 might not be for K^+ and also for organic fragment $C_3H_3^+$ (Silva and Prather, 2000). Especially, the presence of other potassium clusters (i.e., *m/z* $^{113}K_2Cl^+$ or *m/z* $^{213}K_3SO_4^+$) and peaks at *m/z* $^{45}CHO_2^-$, $^{59}C_2H_3O_2^-$ and $^{71}C_3H_3O_2^-$ are distinctive for biomass burning particles (Silva et al., 1999; Dall'Osto et al., 2012). The combination of the presence of phosphate (*m/z* $^{79}PO_3^-$) allows identification of particles derived from traffic emissions.

Particles containing the strongest K^+ (*m/z* $^{39}K^+$) signal in the positive mass spectrum (MS), coexistence significant sulfate (*m/z* $^{97}HSO_4^-$) and nitrate (*m/z* $^{46}NO_2^-$, $^{62}NO_3^-$) fragments in the negative MS are identified as Potassium-rich (K-rich) (Fig. S3a). The sources of the K-rich particles are complex, including biomass burning (Pratt et al., 2011), secondary formation (Bi et al., 2011; Shen et al., 2017), industrial and traffic emissions (Zhang et al., 2017). A weak phosphate (*m/z* $^{79}PO_3^-$) signal can be seen in Fig. S3a, while a study supported that $^{79}PO_3^-$ could be originated from motor vehicle lubricants (Yang et al., 2017). Significant peaks of $^{97}HSO_4^-$ and $^{62}NO_3^-$ indicate that the K-rich particle might also experience atmospheric aging. The particles containing levoglucosan fragments ($^{45}CHO_2^-$, $^{59}C_2H_3O_2^-$, $^{71}C_3H_3O_2^-$, $^{73}C_3HO_3^-$) and $^{113,115}K_2Cl^+$ signals in Fig. S3b are defined as Biomass burning (BB) (Moffet et al., 2008). Organic carbon (OC) particles (Fig.S3c) have strong organic fragments (such as *m/z* $^{27}C_2H_3^+$, $^{37}C_3H^+$, $^{43}C_2H_3O^+$ and $^{51}C_4H_3^+$) in the positive MS, generally from biomass burning and VOCs transformation (Moffet et al., 2008; Bi et al., 2011). Strong $^{97}HSO_4^-$ and $^{62}NO_3^-$ signals in the negative MS represent that the particles have experienced a certain degree of aging in the atmosphere. In addition, $^{79}PO_3^-$ in the negative MS demonstrates the OC is also contributed by traffic emissions. However, the larger molecular weight ions (*m/z* −129, −143) contained in OC negative MS cannot be well interpreted, potentially ascribed to the presence of organosulfates (Hatch et al 2011; Cahill et al., 2012). Notably different from other types of particle, Ammonium particle contains apparent ammonium ions (*m/z* $^{18}NH_4^+$) and amine (*m/z* $^{58}C_2H_5NHCH_2^+$) in the positive MS (Fig. S3d), and strong $^{97}HSO_4^-$ signals in the negative MS. The presence of sulfuric acid (*m/z* $^{195}H(HSO_4)_2^-$) fragments indicates that ammonium is an acidic particle (Rehbein et al., 2011; Lin et al., 2017). There are a variety of sources of ammonium, including sewage treatment, animal husbandry, waste incineration, the marine environment, biomass burning, industrial processes, and vehicle exhaust (Cadle and Mulawa, 1980; Moffet et al., 2008). Moreover, its gaseous precursor of ammonia (NH_3) could be converted into secondary aerosols such as ammonium sulfate/nitrate (Seinfeld and Pandis, 2012; Yang et al., 2012). In this study, ammonium particles show negligible $^{62}NO_3^-$ fragment in the negative MS due to ammonium nitrate being much more volatile and less easily transported than ammonium sulfate (Lall and Thurston 2006; Sun et al. 2012; Xu et al., 2018). These results possibly suggest that ammonium particles have undergone intense atmospheric aging during regional transport. Element carbon (aged EC) particles are characterized by the obvious signals of carbon cluster ions (e.g., *m/z* $^{12}C^{\pm}$, $^{24}C_2^{\pm}$, $^{36}C_3^{\pm}$, $^{48}C_4^{\pm}$, $^{60}C_5^{\pm}$, etc.) and $^{39}K^+$ and $^{97}HSO_4^-$, and also few relatively weak organic fragments (*m/z* $^{27}C_2H_3^+$, $^{43}C_2H_3O^+$) (Fig. S3e) (Moffet and Prather, 2009). The EC-containing particles mainly originated from coal combustion (Bond et al., 2013) and vehicle emissions (Yang et al., 2017). The presence of $^{97}HSO_4^-$ also indicates the aging of the particles. Dust particles mainly contain mineral ions signals in MS (Fig. S3f), such as *m/z* $^{27}Al^+$, $^{40}Ca^+$, $^{56}CaO^+/Fe^+$, $^{16}O^-$, $^{17}OH^-$, $^{76}SiO^-$, and $^{79}PO_3^-$. Different from other particles, the dust particle has no obvious signal of $^{97}HSO_4^-$ and $^{62}NO_3^-$. This could be explained by the dust being much fresh from the local road/construction fly ash or dust events. The characteristic ions of NaK-SN, metal, and other particles are listed in Table 1 and Fig. S3(g,h,i), respectively. Due to their relatively low contributions (< 3%), their recognition is not discussed in detail.

S2. The spatial distribution for the six major particle types

The potential source contribution function (PSCF) model was applied to further identify the spatial distribution of the pollution sources for the six major particle types. For the K-rich and OC particles (Fig. S16), the large fractions in the southwest of Gaomeigu are potentially influenced by biomass burning and traffic emissions, such as the two nearby highways [the Xili Expressway (G0613) and Dali Expressway (G5611)] (Fig. S17). As shown in Fig. S16, the high PSCF values of BB particle are found along Sino-Burmese border and the sampling surroundings. Compared with intensive fire activities (Fig. S18), the contribution of biomass burning particles from long-distance regional transport may be underestimated due to the emitting of levoglucosan ($^{45}CHO_2^-$, $^{59}C_2H_3O_2^-$, $^{71}C_3H_3O_2^-$, $^{73}C_3HO_3^-$) from biomass burning will decaye or even vanish during the atmospheric aging processes (Pratt et al., 2011; Li et al., 2014). Tian et al (2022) also suggested that BBOA was partly aged at Gaomeigu. A higher PSCF value of Ammonium particles is seen in the cross-border of northern Myanmar than in the center of Gaomeigu, representing more influences by transportation than the local emission. Owing to the low consumption of coal in the southeastern Tibet Plateau (Li et al., 2016), the high PSCF values of aged EC particles are more likely from the traffic emissions (Fig. S16). Moreover, sporadic high PSCF values of the aged EC particles are also found in cross-border northern Myanmar, indicating possible influences of biomass burning emissions (Liu et al., 2021). The high PSCF values of Dust particles are observed in the surrounding areas of the southwestern sampling site.

Table S1. Number concentration and relative fraction of the six main particle types in four trajectory clusters during the whole observation.

Type	Cluster 1		Cluster 2		Cluster 3		Cluster 4	
	Counts	Fraction (%)	Counts	Fraction (%)	Counts	Fraction (%)	Counts	Fraction (%)
K-rich	103275	32.7	1486	30.8	33319	26.8	4291	25.2
BB	58379	18.5	1731	35.9	23970	19.3	4562	26.8
OC	37856	12.0	744	15.4	19227	15.5	2138	12.5
Ammonium	39388	12.5	240	5.0	12948	10.4	1304	7.7
Aged EC	35143	11.1	245	5.1	9553	7.7	1077	6.3
Dust	28002	8.9	176	3.6	20613	16.6	2827	16.6

Table S2. Peak searching criteria for selected indicator species.

	Indicator species	*m / z*	Restrictive condition
Secondary organic	$C_2H_3O^+$	43	Relative area > 0.02
	$HC_2O_4^-$	−89	-
Secondary inorganic	NH_4^+	18	Relative area > 0.05
	HSO_4^-	−97	Relative area > 0.1
	NO_3^-	−62	Relative area > 0.1
Primary marker	Cl^-	−35, −37	and
	Levoglucosan	−45, −59, −71	or

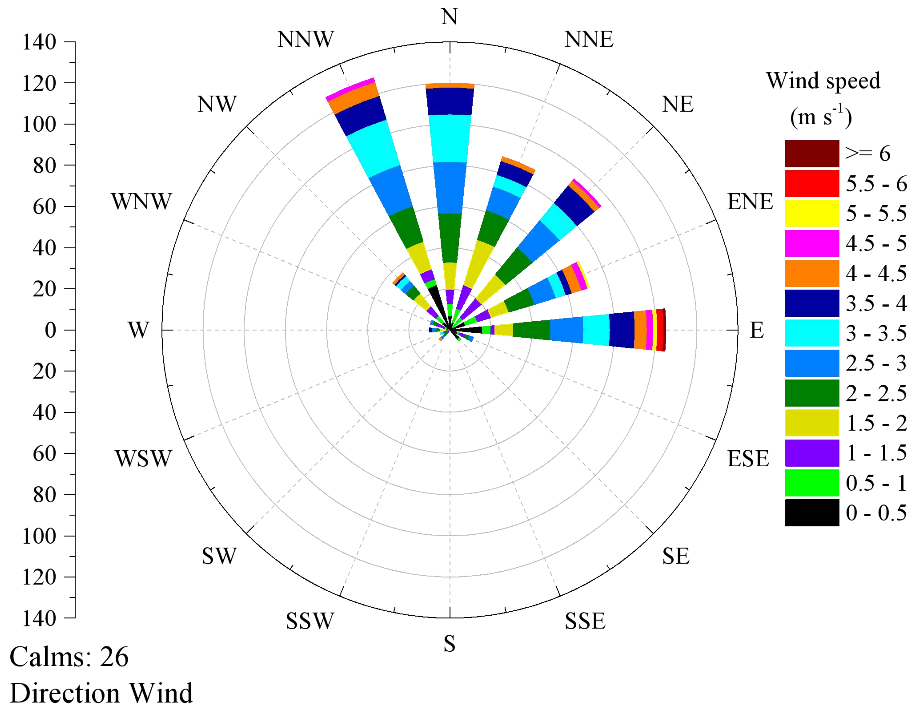

Figure S1. Wind rose of wind direction and wind speed (color bar) during the study period.

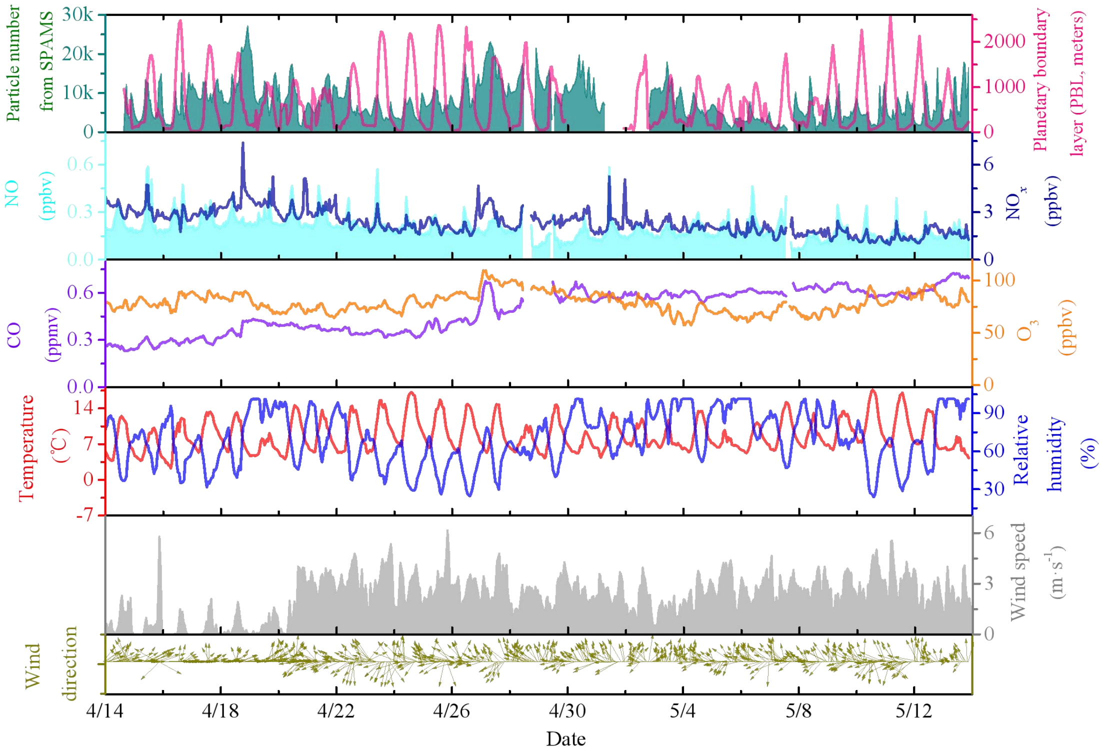

Figure S2. Time series of SPAMS particles, gaseous concentrations (i.e., NO, NO_x, O_3, and CO) and meteorological parameters (planetary boundary layer height, temperature, relative humidity, wind direction, and wind speed).

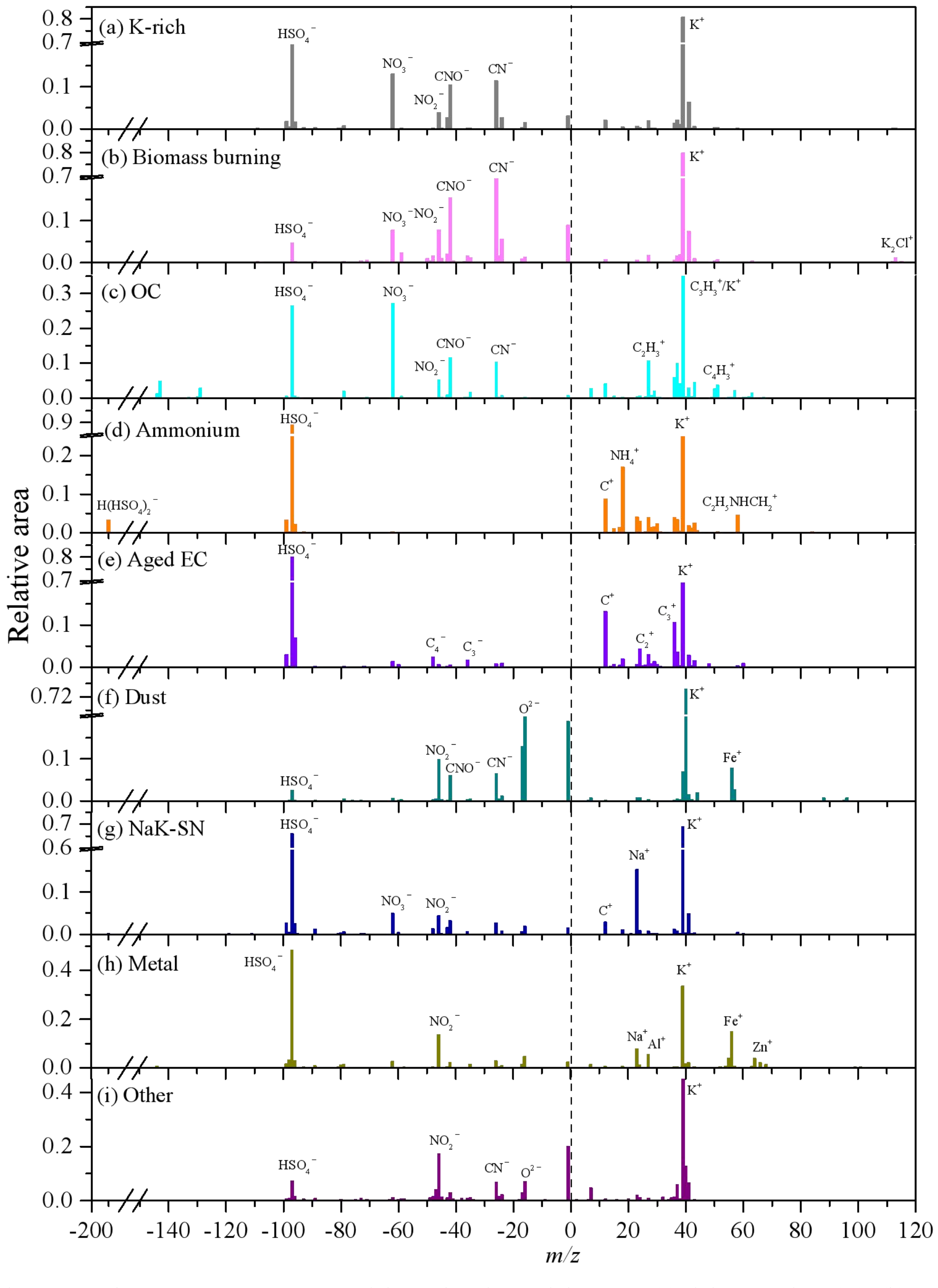

Figure S3. The average mass spectra of the major six particle types: (a) rich-potassium (K), (b) Biomass burning (BB), (c) Organic carbon (OC), (d) Ammonium, (e) Aged element carbon (EC), (f) Dust; and the relatively low contributions (< 3%) types of (g) Sodium, Potassium (NaK)-SN, (h) Metal, (i) Other.

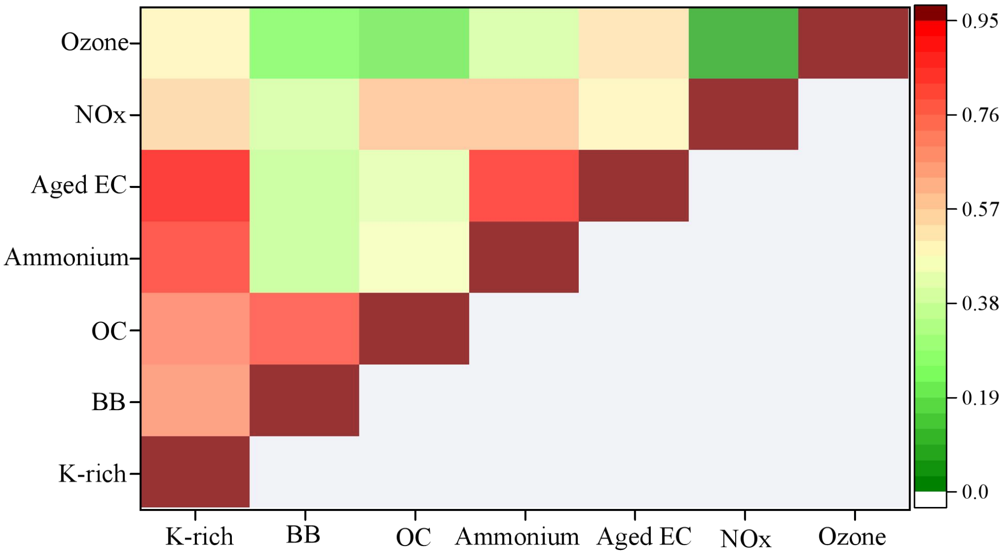

Figure S4. The correlation results between seven variables ($p < 0.01$) was statistically analyzed by IBM SPSS software (version 23). The values in the figure represent Pearson's r.

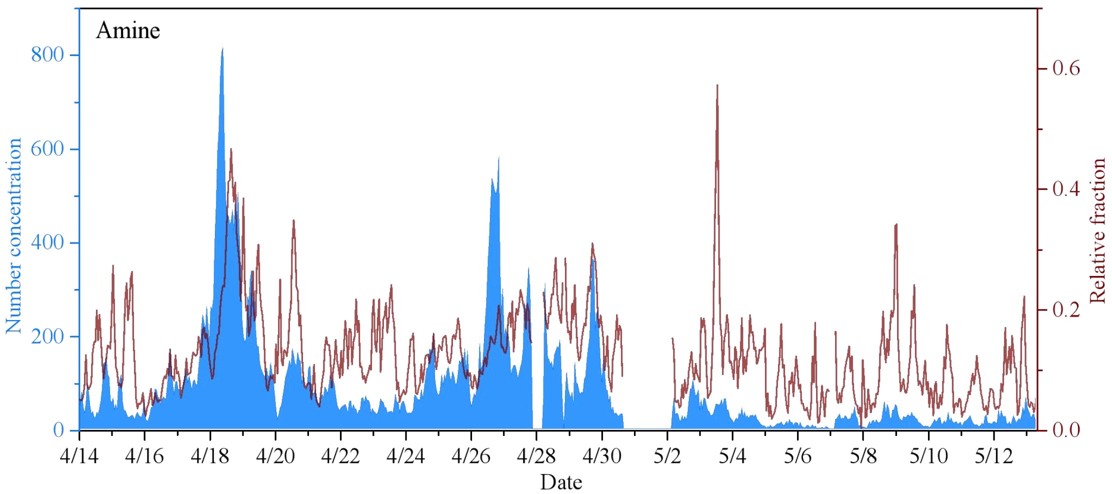

Figure S5. Time-series of the number concentrations (blue area) and the relative fraction (dark red line) of Amine-containing particles during the observation periods.

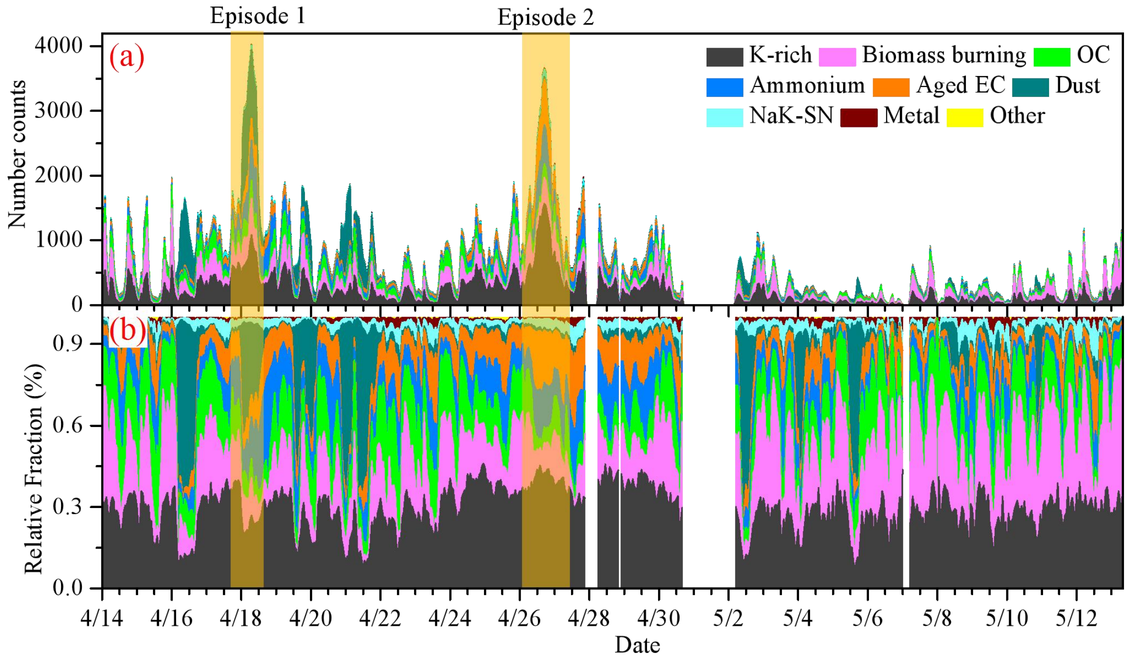

Figure S6. Time-series plots of (a) the number concentrations and (b) the relative fraction of nine particle groups during the observation periods. Particle type abbreviations as in supplementary of section 1. The two yellow shades regions correspond to Episode 1 and 2, respectively.

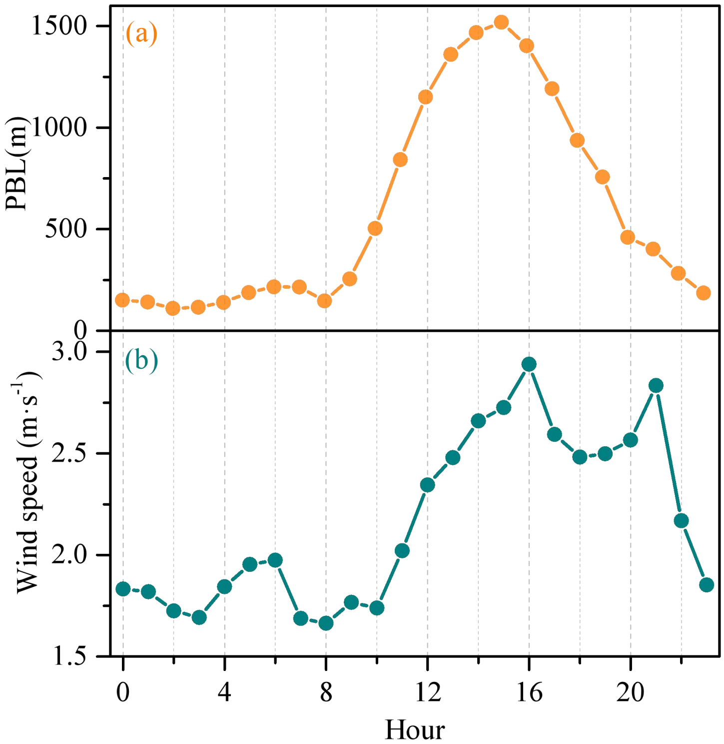

Figure S7. Diurnal variation of the (a) planetary boundary layer (PBL) and (b) wind speed (WS) during the entire observation period.

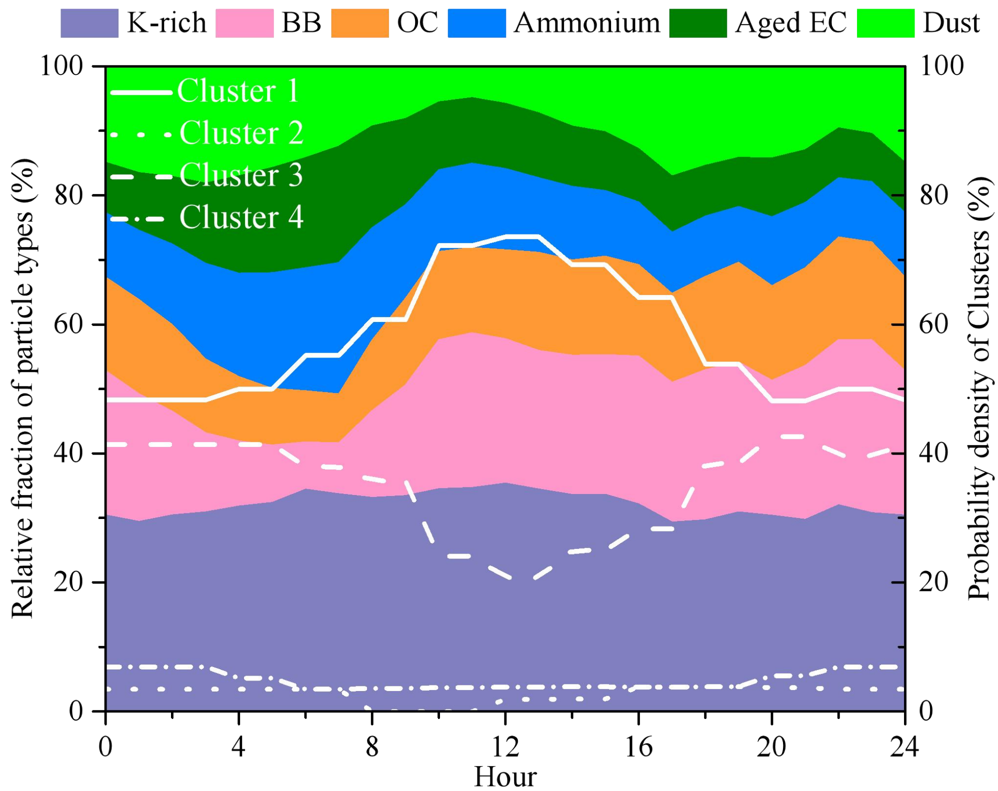

Figure S8. Diurnal variation of the relative fraction of the six major particle types and the probability density of the four clusters during entire observation period. The white lines represent the probability densities for the four air clusters.

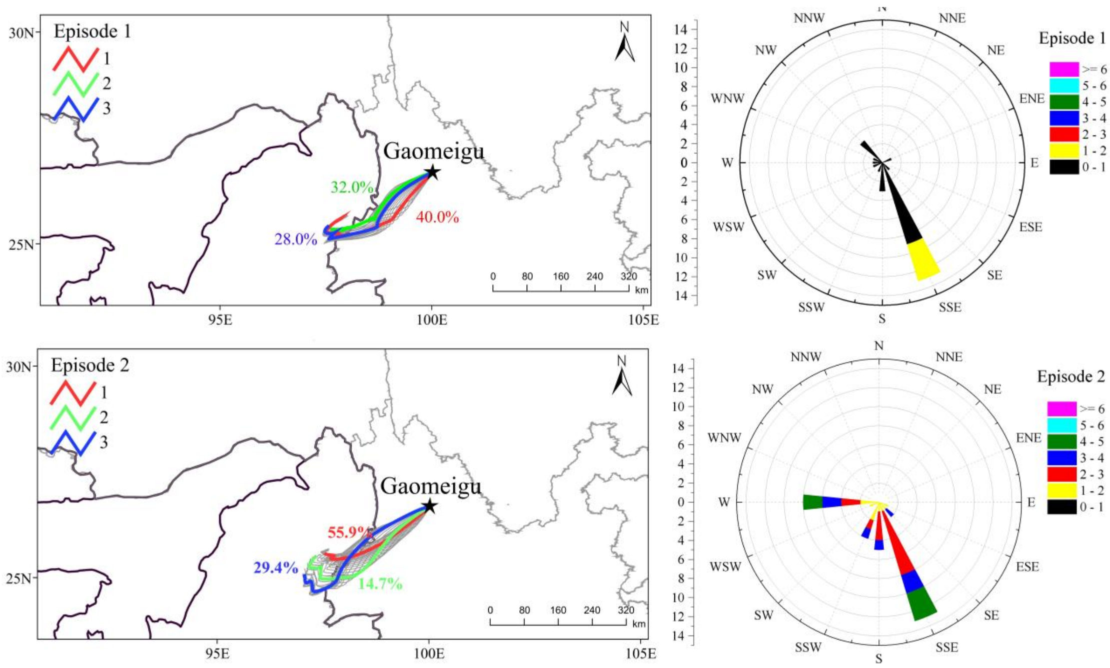

Figure S9. Maps of the mean HYSPLIT back trajectory clusters (72 h) at the height of 500 m during the Episode 1 (from 08:00 LT April 18th to 08:00 LT April 19th 2019) and Episode 2 (from 17:00 LT April 26th to 02:00 LT April 28th), and the wind speed and direction.

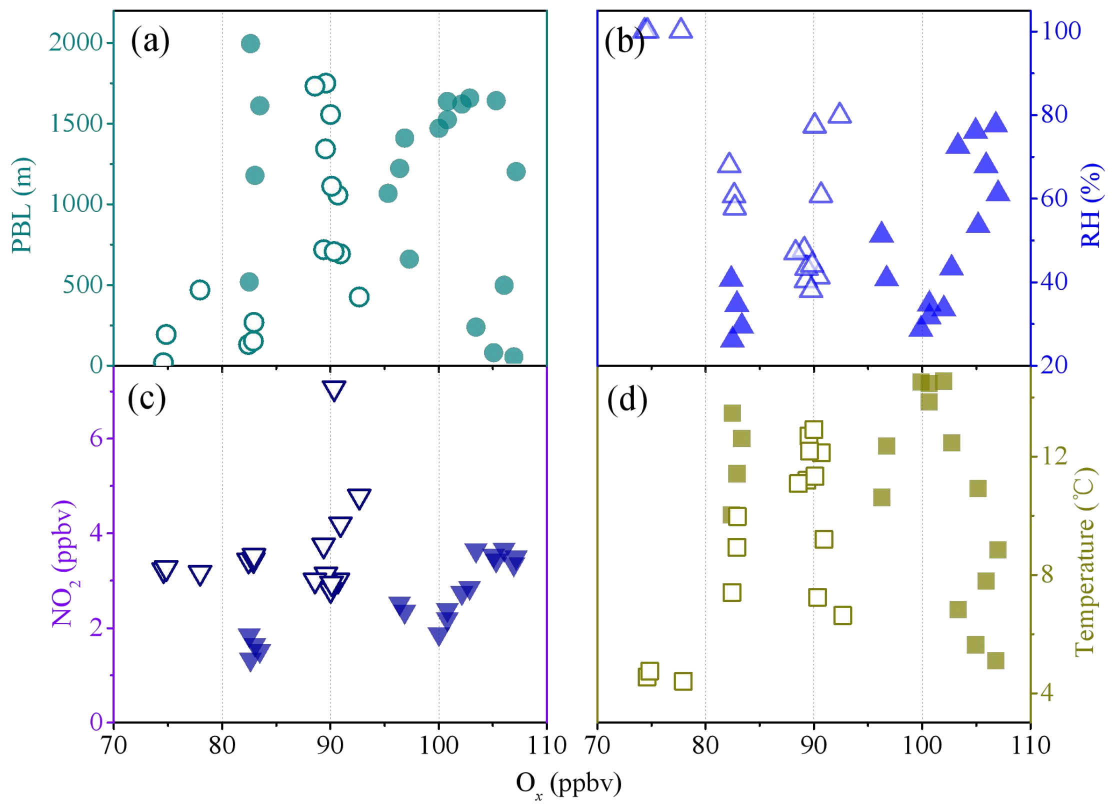

Figure S10. Correlations between oxidant (O_x) concentration and (a) PBL, (b) RH, (c) NO_2 concentration, and (d) temperature during the Episode 1 (the open shape) and Episode 2 (the solid shape).

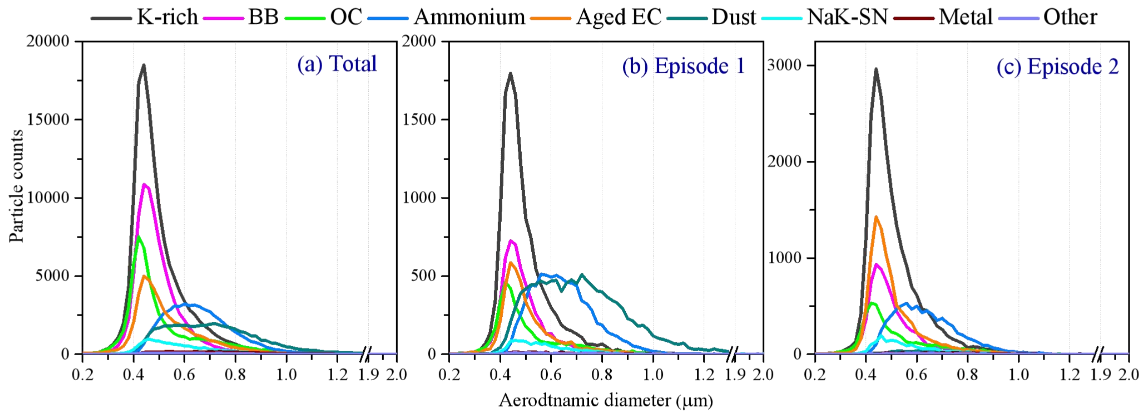

Figure S11. SPAMS-specific size distributions of the number concentrations of the nine particle types during (a) the total observation periods and two episodes of (b) E1 and (c) E2.

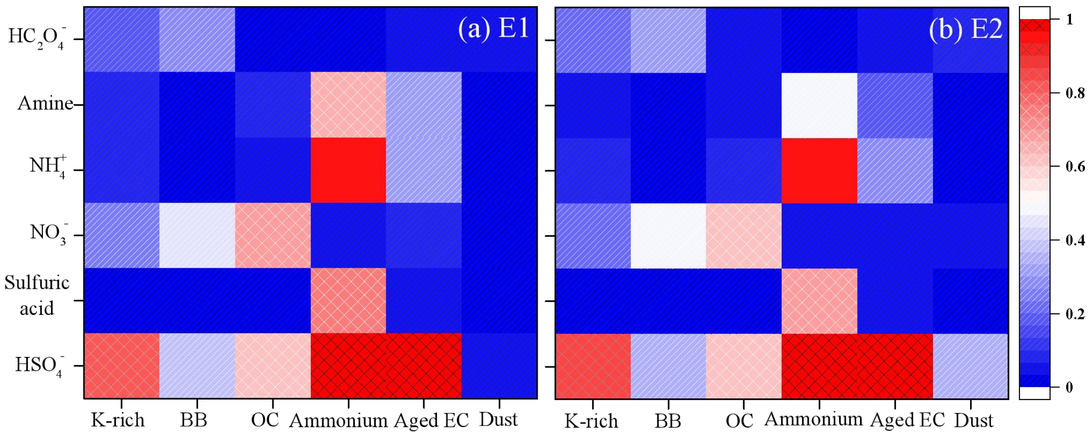

Figure S12. Number fractions of secondary markers associated with the six particle types (K-rich, BB, OC, ammonium, aged EC, dust) in two episodes of E1 and E2: sulfate ($^{97}HSO_4^-$), sulfuric acid ($^{195}H(HSO_4)_2^-$), nitrate ($^{62}NO_3^-$), ammonium ($^{18}NH_4^+$), amine ($^{58}C_2H_5NHCH_2^+$), and oxalate ($^{89}HC_2O_4^-$).

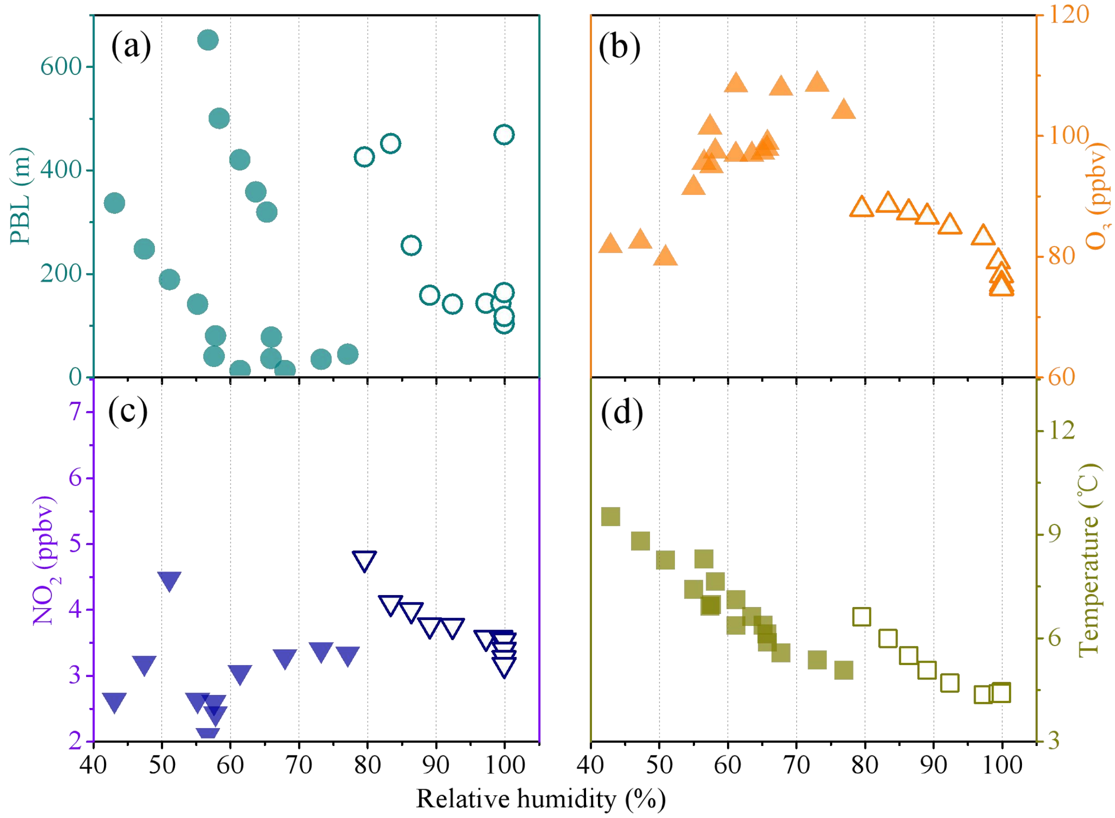

Figure S13. Correlations between RH and (a) PBL height, (b) O_3 concentration, (c) NO_2 concentration, and (d) temperature during the Episode 1 (the open shape) and Episode 2 (the solid shape).

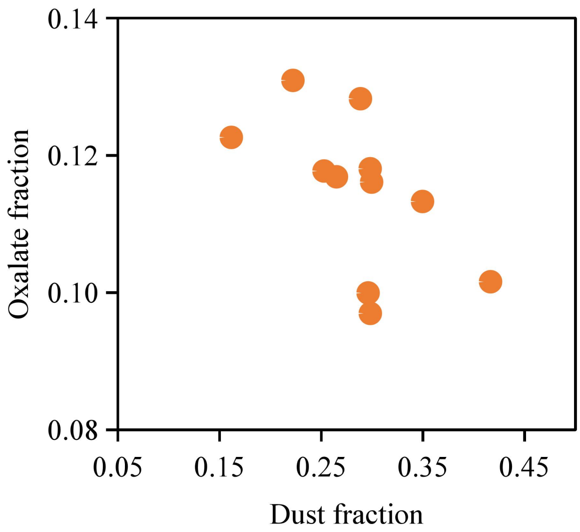

Figure S14. Correlations between the relative fraction of oxalate and Dust type during E1.

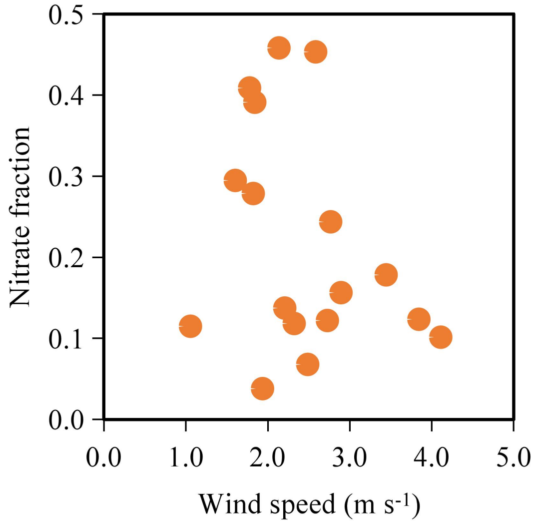

Figure S15. Correlations between the relative fraction of nitrate ($^{62}NO_3^-$) and wind speed during E2.

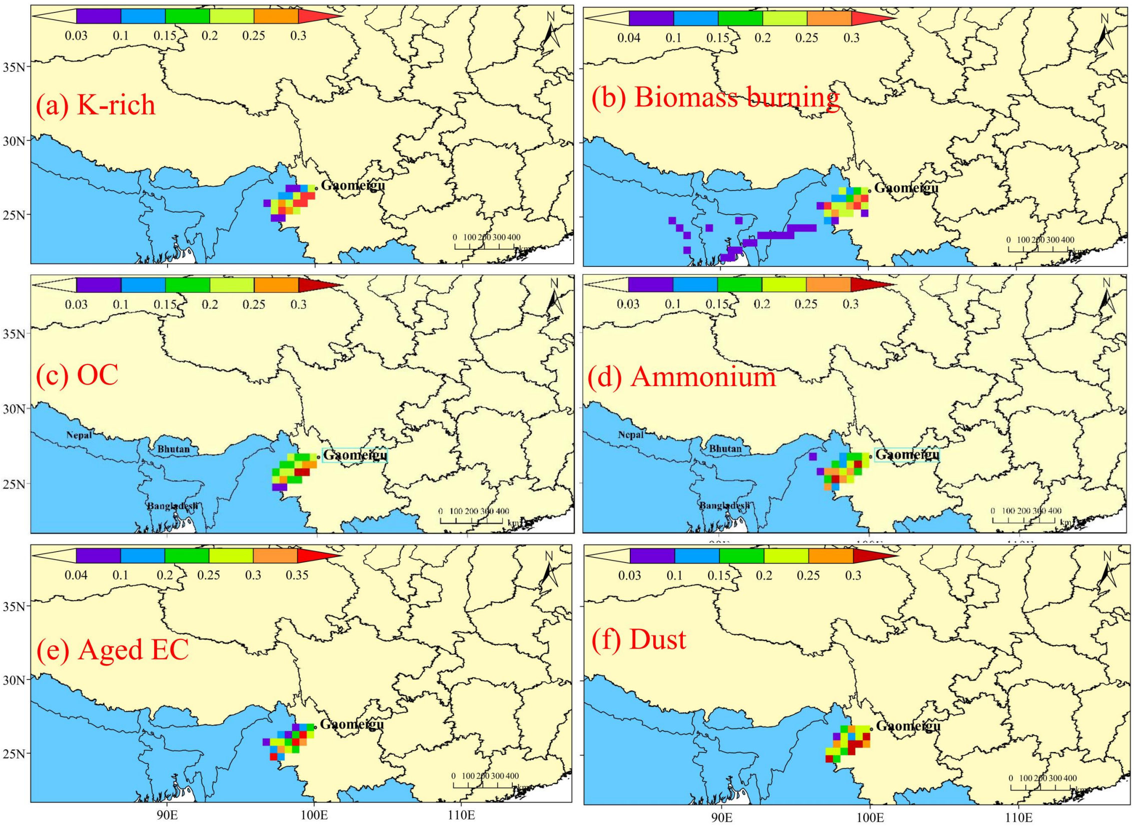

Figure S16. Maps of the potential source contribution functions for (a) K-rich, (b) Biomass burning, (c) OC, (d) Ammonium, (e) Aged EC, and (f) Dust particles; the 75th percentile was 309, 194, 127, 101, 84 and 84, respectively.

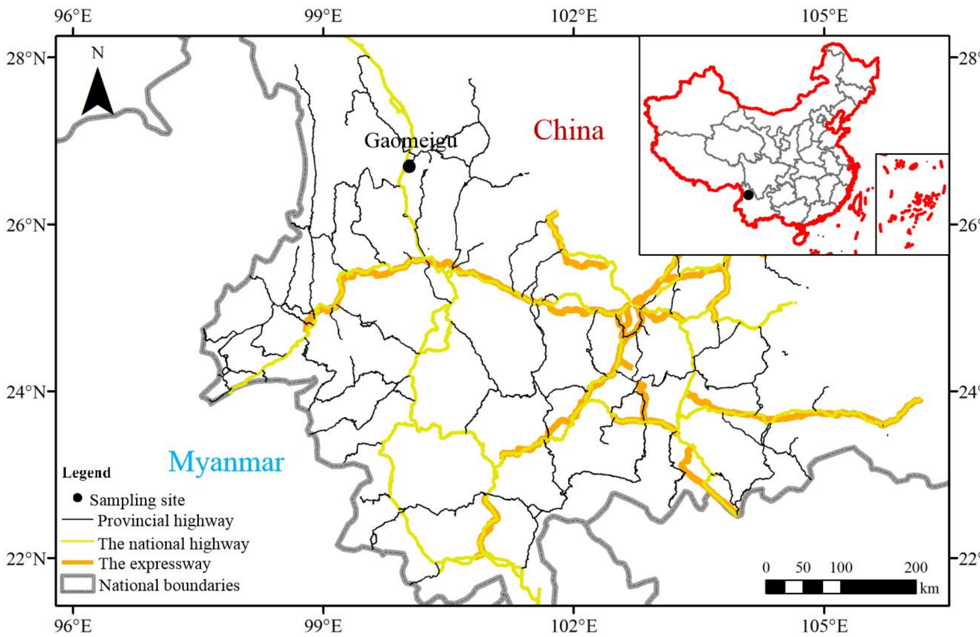

Figure S17. Map of highway distribution near sampling sites from ArcGis10.6 software; dataset acquired from Global Roads Inventory Project (GRIP): global roads database (https://www.globio.info/resources). The GRIP dataset consists of global and regional vector datasets in ESRI filegeodatabase and shapefile format, and global raster datasets of road density at a 5 arcminutes resolution (~8×8km).

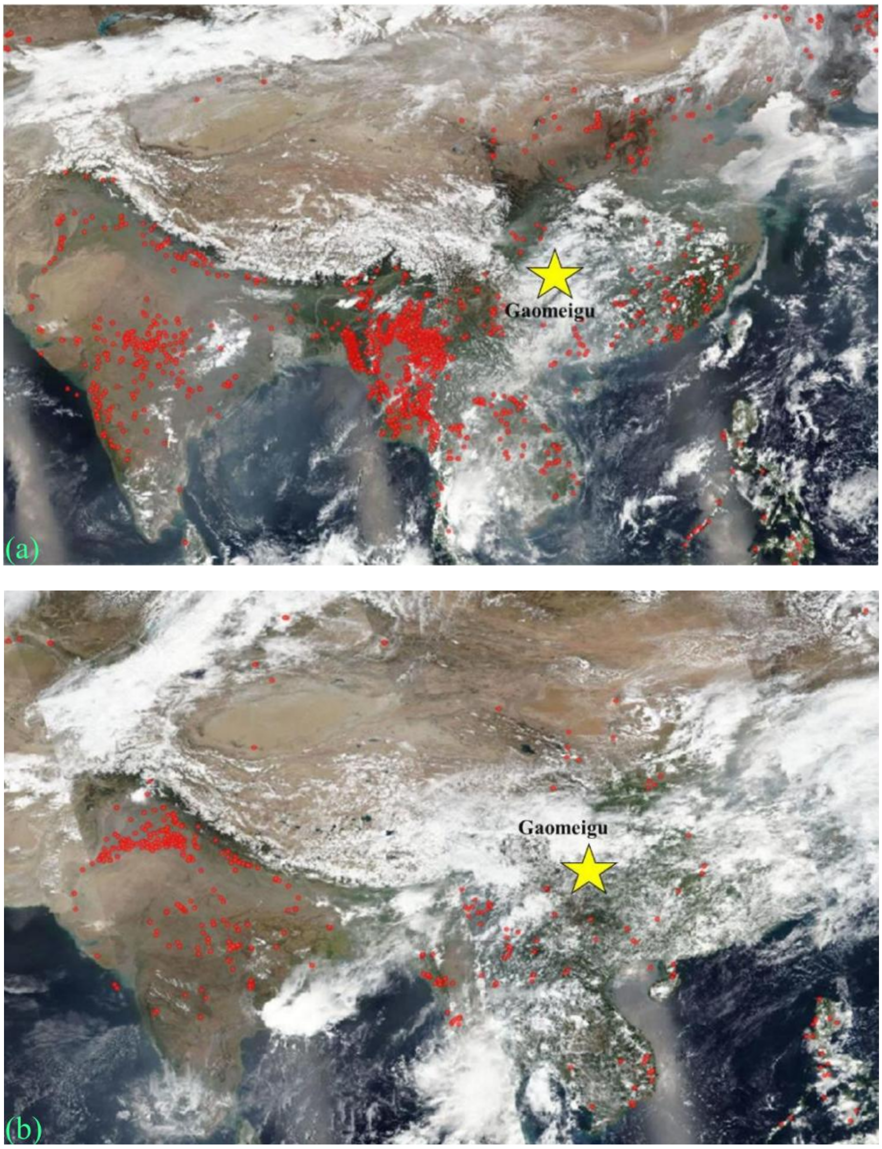

Figure S18. Monthly average fire site maps for (b) April 2018, and (c) May 2018. The fire site maps are from © NASA (National Aeronautics and Space Administration) (https://www.nasa.gov/image-feature/goddard/2018/a-world-on-fire).

Reference

Bi, X. H., Zhang, G. H., Li, L., Wang, X. M., Li, M., Sheng, G. Y., Fu, J. M., and Zhou, Z.: Mixing state of biomass burning particles by single particle aerosol mass spectrometer in the urban area of PRD, China, Atmos. Environ., 45, 3447–3453, https://doi.org/10.1016/j.atmosenv.2011.03.034, 2011.

Bond, T. C., Doherty, S. J., Fahey, D. W., Forster, P. M., Berntsen, T., DeAngelo, B. J., Flanner, M. G., Ghan, S., Kärcher, B., Koch, D., Kinne, S., Kondo, Y., Quinn, P. K., Sarofim, M. C., Schultz, M. G., Schulz, M., Venkataraman, C., Zhang, H., Zhang, S., Bellouin, N., Guttikunda, S. K., Hopke, P. K., Jacobson, M. Z., Kaiser, J. W., Klimont, Z., Lohmann, U., Schwarz, J. P., Shindell, D., Storelvmo, T., Warren, S. G., and Zender, C. S.: Bounding the role of black carbon in the climate system: a scientific assessment, J. Geophys. Res. Atmos., 118, 5380–5552, ,https://doi.org/10.1002/jgrd.50171, 2013.

Cadle, S. H., and Mulawa, P. A.: Low-molecular-weight aliphatic amines in exhaust from catalyst-equipped cars, Environ. Sci. Technol., 14 (6), 718–723, https://doi.org/10.1021/es60166a011, 1980.

Cahill, J. F., Suski, K., Seinfeld, J. H., Zaveri, R. A., and Prather, K. A.: The mixing state of carbonaceous aerosol particles in northern and southern California measured during CARES and CalNex 2010, Atmos. Chem. Phys., 12, 10989–11002, https://doi.org/10.5194/acp-12-10989-2012, 2012.

Dall'Osto, M., and Harrison, R. M.: Urban organic aerosols measured by single particle mass spectrometry in the megacity of London, Atmos. Chem. Phys., 12, 4127–4142, https://doi.org/10.5194/acp-12-4127-2012, 2012.

Gross, D. S., Gälli, M. E., Siliva, P. J., and Prather, K. A.: Relative sensitivity factors for alkali metal and ammonium cations in single-particle aerosol time-of-flight mass spectra, Anal. Chem., 72, 416–422, https://doi.org/10.1021/ac990434g, 2000.

Giorio, C., Tapparo, A., Dall'Osto, M., Beddows, D. C. S., Esser-Gietl, J. K., Healy, R. M., and Harrison, R. M.: Local and Regional Components of Aerosol in a Heavily Trafficked Street Canyon in Central London Derived from PMF and Cluster Analysis of Single-Particle ATOFMS Spectra, Environ. Sci. Technol., 49(6), 3330–3340, https://doi.org/10.1021/es506249z, 2015.

Hatch, L. E., Creamean, J. M., Ault, A. P., Surratt, J. D., Chan, M. N., Seinfeld, J. H., Edgerton, E. S., Su, Y., Prather, K. A.: Measurements of Isoprene-Derived Organosulfates in Ambient Aerosols by Aerosol Time-of-Flight Mass Spectrometry–Part1: Single Particle Atmospheric Observations in Atlanta, Environ. Sci. Technol., 45, 5105–5111, https://doi.org/10.1021/es103944a, 2011.

Healy, R. M., Sciare, J., Poulain, L., Crippa, M., Wiedensohler, A., Prévôt, A.S.H., Baltensperger, U., Sarda-Estève, R., McGuire, M. L., Jeong, C. H., McGillicuddy, E., O'Connor, I. P., Sodeau, J. R., Evans, G. J., and Wenger, J. C.: Quantitative determination of carbonaceous particle mixing state in Paris using single-particle mass spectrometer and aerosol mass spectrometer measurements, Atmos. Chem. Phys., 13, 9479–9496, http://dx.doi.org/10.5194/acp-13-9479-2013, 2013.

Lall, R., and Thurston, G.D.: Identifying and quantifying transported vs. local sources of new York City $PM_{2.5}$ fine particulate matter air pollution, Atmos Environ., 40, 333–346, https://doi.org/10.1016/j.atmosenv.2006.04.068, 2006.

Li, L., Li, M., Huang, Z. X., Gao, W., Nian, H. Q., Fu, Z., Gao, J., Chai, F. H., and Zhou, Z.: Ambient particle characterization by single particle aerosol mass spectrometry in an urban area of Beijing, Atmos. Environ., 94, 323–331, https://doi.org/10.1016/j.atmosenv.2014.03.048, 2014.

Li, C. L., Bosch, C., Kang, S. C., Andersson, A. Chen., P. F., Zhang, Q. G., Cong., Z. Y., Chen, B., Qin., D. H., and Gustafsson., Ö.: Sources of black carbon to the Himalayan–Tibetan Plateau glaciers, Nat. Commun., 7, 12574, https://doi.org/10.1038/ncomms12574,, 2016.

Lin, Q. H., Zhang, G. H., Peng, L., Bi, X. H., Wang, X. M., Brechtel, F. J., Li, M., Chen, D. H., Peng, P. A., Sheng, G. Y., Zhou, Z.: In situ chemical composition measurement of individual cloud residue particles at a mountain site, southern China, Atmos. Chem. Phys., 17, 8473–8488, https://doi.org/10.5194/acp-17-8473-2017, 2017.

Liu, H. K., Wang, Q. Y., Xing, L., Zhang, Y., Zhang, T., Ran, W. K., and Cao, J. J.: Measurement report: quantifying source contribution of fossil fuels and biomass-burning black carbon aerosol in the southeastern margin of the Tibetan Plateau, Atmos. Chem. Phys., 21, 973–987, https://doi.org/10.5194/acp-21-973-2021, 2021.

Moffet, R. C., Foy, B. D., Molina, L. A., Molina, M. J., Prather, K. A.: Measurement of ambient aerosols in northern Mexico City by single particle mass spectrometry. Atmos. Chem. Phys., 8 (16), 4499–4516, https://doi.org/10.5194/acpd-7-6413-2007, 2008.

Moffet, R. C., and Prather, K.A.: In-situ measurements of the mixing state and optical properties of soot with implications for radiative forcing estimates, P. Natl. Acad. Sci. USA, 106, 11872–11877, https://doi.org/10.1073/pnas.0900040106, 2009.

Pratt, K. A., Murphy, S. M., Subramanian, R., DeMott, P. J., Kok, G. L., Campos, T., Rogers, D. C., Prenni, A. J., Heymsfield, A. J., Seinfeld, J. H., and Prather, K. A.: Flight-based chemical characterization of biomass burning aerosols within two prescribed burn smoke plumes, Atmos. Chem. Phys., 11, 12549–12565, https://doi.org/10.5194/acp-11-12549-2011, 2011.

Rehbein, P. J., Jeong, C. H., McGuire, M. L., Yao, X., Corbin, J. C., and Evans, G. J.: Cloud and fog processing enhanced gas-toparticle partitioning of trimethylamine, Environ. Sci. Technol., 45, 4346–4352, https://doi.org/10.1021/es1042113, 2011.

Seinfeld, J. H., and Pandis, S. N.: Atmospheric Chemistry and Physics: from Air Pollution to Climate Change, John Wiley & Sons., 1326. https://doi.org/10.1080/00139157.1999.10544295, 2012.

Shen, L. J., Wang, H. L., Lü, S., Zhang, X. H., Yuan, J., Tao, S. K., Zhang, G. J., Wang, F., and Li, L.: Influence of pollution control on air pollutants and the mixing state of aerosol particles during the 2nd World Internet Conference in Jiaxing, China, J. Clean. Prod., 149, 436–447, https://doi.org/10.1016/j.jclepro.2017.02.114, 2017.

Silva, P. J., Liu, D.Y., Noble, C.A., and Prather, K. A.: Size and chemical characterization of individual particles resulting from biomass burning of local Southern California species, Environ. Sci. Technol., 33, 3068–3076, https://doi.org/10.1021/es980544p, 1999.

Silva, P. J. and Prather K. A.: Interpretation of mass spectra from organic compounds in aerosol time-of-flight mass spectrometry, Anal. Chem., 72, 3553–3562, https://doi.org/10.1021/ac9910132, 2000.

Sun, Y. L., Zhang, Q., Schwab, J. J., Yang, T., Ng, N. L., and Demerjian, K. L.: Factor analysis of combined organic and inorganic aerosol mass spectra from high resolution aerosol mass spectrometer measurements, Atmos. Chem. Phys., 12, 8537–8551, https://doi.org/10.5194/acp-12-8537-2012, 2012.

Xu, J., Li, M., Shi, G., Wang, H., Ma, X., Wu, J., Shi, X., and Feng, Y.: Mass spectra features of biomass burning boiler and coal burning boiler emitted particles by single particle aerosol mass spectrometer, Sci. Total Environ., 598, 341–352, https://doi.org/10.1016/j.scitotenv.2017.04.132, 2017.

Xu, L. L., Wu, X., Hong, Z. Y., Zhang, Y. R., Deng, J. J., Hong, Y. W., and Chen, J. S.: Composition, mixing state, and size distribution of single submicron particles during pollution episodes in a coastal city in southeast China, Environ. Sci. Pollut. Res., 26, 1464–1473, https://doi.org/10.1007/s11356-018-3469-x, 2018.

Yang, J., Ma, S. X., Gao, B., Li, X. Y., Zhang, Y. J., Cai, J., Li, M., Yao, L. A., Huang, B., and Zheng, M.: Single particle mass spectral signatures from vehicle exhaust particles and the source apportionment of on-line $PM_{2.5}$ by single particle aerosol mass spectrometry, Sci. Total Environ., 593, 310–318, https://doi.org/10.1016/j.scitotenv.2017.03.099, 2017.

Yang, F., Chen, H., Du, J., Yang, X., Gao, S., Chen, J., and Geng, F.: Evolution of the mixing state of fine aerosols during haze events in Shanghai, Atmos. Res., 104, 193–201, https://doi.org/10.1016/j.atmosres.2011.10.005, 2012.

Zhang, J. K., Luo, B., Zhang, J. Q., Ouyang, F., Song, H. Y., Liu, P. C., Cao, P., Schäfer, K., Wang, S. G., Huang, X. J., and Lin, Y. F.: Analysis of the characteristics of single atmospheric particles in Chengdu using single particle mass spectrometry, Atmos. Environ., 157, 91–100, https://doi.org/10.1016/j.atmosenv.2017.03.012, 2017.